Volume 14, Issue 4, 142442 (1-14)

Iranian Journal of Catalysis (IJC)

https://doi.org/10.57647/j.ijc.2024.1404.42

Preparation of heterostructure Pt/Bi_2MoO_6 nanocomposites by microwave-assisted deposition method for using as a visible-light-driven photocatalyst

Soraya Pinchujit[1], Anukorn Phuruangrat[1*], Surangkana Wannapop[2], Titipun Thongtem[3,4], Somchai Thongtem[*3,5]

[1]*Division of Physical Science, Faculty of Science, Prince of Songkla University, Hat Yai, Songkhla,Thailand.*
[2]*Faculty of Science, Energy and Environment, King Mongkut's University of Technology, North Bangkok, Rayong Campus, Rayong, Thailand.*
[3]*Materials Science Research Center, Faculty of Science, Chiang Mai University, Chiang Mai, Thailand.*
[4]*Department of Chemistry, Faculty of Science, Chiang Mai University,Chiang Mai, Thailand.*
[5]*Department of Physics and Materials Science, Faculty of Science, Chiang Mai University, Chiang Mai, Thailand.*

[*]**Corresponding authors:** phuruangrat@hotmail.com, schthongtem@yahoo.com

Original Research

Received:
24 April 2024
Revised:
16 August 2024
Accepted:
2 October 2024
Published online:
16 October 2024

Abstract:

Heterostructure Pt/Bi_2MoO_6 nanocomposites containing different weight contents of Pt nanoparticles were successfully synthesized by an effective microwave-assisted deposition method. The effect of Pt contents loaded on the Bi_2MoO_6 nanoplates was investigated through the photodegradation of rhodamine B (RhB) illuminated by visible radiation. Face-centered cubic (FCC) metallic Pt nanoparticles were supported on the surface of orthorhombic Bi_2MoO_6 nanoplates with very good distribution by a microwave-assisted deposition method. The photocatalytic performance of Bi_2MoO_6 nanoplates was increased with increasing the loaded Pt nanoparticles from 1% to 10%. Upon further increasing the loaded Pt nanoparticles to 15%, the photocatalytic performance for the degradation of RhB was significantly reduced. In this research, 10% Pt/Bi_2MoO_6 nanocomposites have the highest photocatalytic activity because Pt nanoparticles are very good electrical conductors that play the role of enhancing photocatalytic reaction rate.

Keywords: Active radicals; Pt/Bi_2MoO_6 nanocomposites; Photocatalytic reaction; Rhodamine B

1. Introduction

Organic dyes from textile, paint, food, leather, paper, and pharmaceutical industries contain complex constituents with one or more benzene rings. They are very high toxic materials with slow decomposition rate and can play the role in affecting human health, plants and organism lives in water [1–5]. Rhodamine B (RhB), a xanthene dye, is widely used as a fluorescent agent in biological and fluorescent applications, including colorant in textile, plastic, glass, and firework industries. These dyes were found in wastewater because of their high solubility and have been listed as toxic and carcinogenic agents by the International Agency for Research on Cancer (IARC) and the European Food Safety Authority (EFSA) [6–8]. They can lead to cause different diseases in humans and organisms by inducing mutagenicity and carcinogenicity [6–8]. Traditional wastewater treatment, including biological process, physical/chemical adsorption, precipitation, and flocculation, are quite disadvantageous and are used to remove organic pollutants in wastewater because these methods are expensive and complex, including the creation of secondary waste and limitations in practical application [1, 3, 4]. The photocatalytic semiconductors, the promising wastewater treatment agents, play the role of generating highly reactive oxidative species under light irradiation. These reactive oxidative species can completely

degrade toxic organic pollutants by transforming them into harmless compounds [5, 9–16].

Bismuth molybdate (Bi_2MoO_6) with band gap energy of 2.5–2.8 eV is composed of $[Bi_2O_2]^{2+}$ layers interleaved by alternately stacked double slabs of $[MoO_4]^{2-}$ perovskite layers. It is a promising candidate photocatalyst used for the degradation of organic pollutants under visible radiation [1, 9, 17–20]. The hydrothermal method was selected and used to prepare Bi_2MoO_6 photocatalyst because the synthetic process is mild, low cost, and facile. The synthesized products have a high degree of crystallinity, high purity, narrow particle-size distribution, and low aggregation [21–23]. Nevertheless, the practical application in degrading organic pollutants was limited by poor quantum yield, rapid recombination of photo-excited carrier pairs, and slow carrier diffusion rate [9, 16–18, 24–26]. A number of noble metals such as Pd [19, 27], Ag [28, 29], Ru [30, 31], and Au [32, 33] were deposited on the photocatalytic semiconductor to enhance photocatalytic activity by increasing photogenerated charge carrier diffusion rate and charge separation between semiconductor and metal. Therefore, the recombination of the charge carriers was reduced, and the lifetime was extended by constructing the Schottky barrier at the metal/semiconductor interface [19, 27, 29, 34, 35]. The noble metal nanoparticles modified on the semiconductor can lead to effectively harvest more visible light by surface plasmon resonance (SPR) effect and promote electron diffusion at the metal-semiconductor interface [19, 27–29, 36]. Among them, Pt nanoparticles are effectively loaded noble metals for improving oxide semiconductors and act as the conductor of photogenerated electrons. Thus, the absorption of visible light was increased by localized surface plasmon resonance (LSPR) effect and played the role in effective promoting the separation of photogenerated charge carriers [37–39]. Deposition by microwave was used to produce metallic nanoparticles supported on semiconductors such as Ag/ZnO [40, 41], Ag/BiOCl [42], Ag/graphene oxide [43], Pd/graphite [44], Pt/reduced graphene oxide [44], Pd/Fe_3O_4/zeolitic imidazolate frameworks [45], Pt/-graphitic carbon [46], Pt/graphene [47], Pt/SnO_2 [48] and PtCo/carbon nanotubes [49] because this method is fast, no selective heating, energy-saving, short reaction time and inexpensive. The product has a high yield and narrow particle-size distribution and is very pure with no aggregation of nanoparticles as compared to the traditional coating method [50, 51].

In this study, heterostructure Pt/Bi_2MoO_6 nanocomposites were successfully prepared using an effective microwave-assisted deposition method. Microwave-assisted deposition is a candidate method for transforming metallic ions into uniform and homogenous metallic nanoparticles on the semiconductor materials containing in the solution. Bi_2MoO_6 sample and heterostructure Pt/Bi_2MoO_6 nanocomposites were characterized by different techniques to study phase, morphology, the oxidation state of an element, surface area, and optical properties. The effect of the weight percent of Pt loaded on the synthetic products was investigated through the degradation of rhodamine B (RhB) under visible light irradiation. Active radicals were investigated by a trapping test. The photocatalytic recyclability and stability of heterostructure Pt/Bi_2MoO_6 nanocomposites were also studied and discussed according to the experimental results.

2. Experiment

2.1 Synthesis of heterostructure Pt/Bi_2MoO_6 nanocomposites

To prepare Bi_2MoO_6 nanoplates by hydrothermal method, 0.01 mol $Bi(NO_3)_3$_$5H_2O$ and 0.005 mol Na_2MoO_4_$2H_2O$ were dissolved in 100 ml reverse osmosis (RO) water and followed by adjusting the pH of 6 by 3 M NaOH. The solution system was put in a 200 ml Teflon-lined stainless steel autoclave, which was heated at 180 oC for 20 h. The as-prepared precipitates were collected, washed, and dried for future preparation of heterostructure Pt/Bi_2MoO_6 nanocomposites. Each of 1wt%, 5wt%, 10wt%, and 15wt% H_2PtCl_6_xH_2O was dissolved in 100 ml ethylene glycol, which was stirred for homogeneity. Subsequently, each 2.50 g Bi_2MoO_6 powder was added to these homogeneous solutions. The system was heated by microwave at 300 W for 20 min to form heterostructure Pt/Bi_2MoO_6 nanocomposites. In the end, the samples were collected, washed, and dried for further characterization. The synthetic process of the samples is shown in Fig. 1.

2.2 Characterization

Phase and structure of Bi_2MoO_6 and Pt/Bi_2MoO_6 were investigated by an X-ray diffractometer (Philips X'Pert MPD, XRD) by monochromatic Cu Kα as an X-ray source at a scanning rate of $0.01^o.s^{-1}$ with 2θ range of 10–60^o. The atomic vibration of samples was operated on a Fourier transform infrared spectrometer (BRUKER TENSOR 27, FTIR) and a Raman spectrometer (HORIBA JOBIN YVON T64000) at 50 mW Ar green laser of 514.5nm wavelength. A JEOL JSM 6335F scanning electron microscope (SEM) combined with an Oxford INCA energy dispersive spectrometer (EDS) using a Si(Li)-type detector operating at 35 kV was used to analyze the morphology and element of the samples. The interface of Pt and Bi_2MoO_6 was analyzed by transmission electron microscopy (JEOL JEM-2010, TEM) using LaB_6 as an electron gun at 200 kV. An X-ray photoelectron spectrophotometer (XPS) was operated on Axis Ultra DLD, Kratos Analytical Ltd by monochromatic Al Kα radiation at 1486.6 eV and C 1s at 285.1 eV for calibration. The optical properties of Bi_2MoO_6 and Pt/Bi_2MoO_6 were performed by a Shimadzu UV-2600 UV-visible diffuse reflectance spectrometer (UV-vis DRS) with $BaSO_4$ standard reference at 200–800 nm. The specific surface area of the sample was analyzed by a Micromeritics TriStar II 3020 analyzer.

2.3 Photodegradation experiment

0.2 g Pt/Bi_2MoO_6 suspension containing in 200 ml of 1×10^{-5} M RhB solution was magnetically stirred in the dark condition for 30 min. Subsequently, the solution with constant stirring was illuminated by the visible light of a xenon lamp, and 5 ml RhB solution was sampled every 30 min interval. The residual content of RhB after the photo-

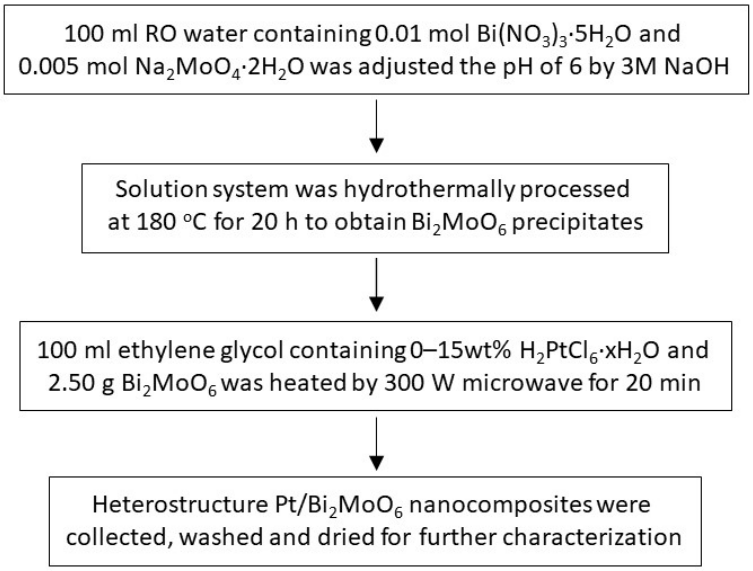

Figure 1. Schematic diagram for the synthesis of heterostructure Pt/Bi_2MoO_6 nanocomposites.

catalytic reaction was analyzed at the maximum absorption wavelength (λ_{max} = 554 nm) by a Perkin Elmer, Lambda 25 UV/Vis spectrometer. The decolorization efficiency for RhB degradation over the photocatalyst was calculated using the following Eq. 1:

$$\text{Decolorization efficiency}(\%) = \frac{C_0 - C_t}{C_0} \times 100 \quad (1)$$

Co is the initial content of RhB and Ct is the content of RhB after light irradiation within a period of time (t). In the end, the degraded RhB solution at t = 0, 60 and 120 min over 10%Pt/Bi_2MoO_6 were studied by a liquid chromatography-quadrupole time-of-flight mass spectrometer (LC-QTOF MS) on 1290 Infinity II LC-6545 Quadrupole-TOF, Agilent Technologies using a positive electrospray ionization (ESI^+) mode.

3. Results and discussion

3.1 Characterization of heterostructure Pt/Bi_2MoO_6 nanocomposites

Fig. 2 shows XRD patterns of Bi_2MoO_6 with and without the loaded Pt. The XRD pattern of the Bi_2MoO_6 sample without the loaded Pt prepared by a simple hydrothermal method was indexed to the orthorhombic Bi_2MoO_6 structure with space group of Pna21 (JCPDS No. 21-0102 [52]). The XRD patterns of Bi_2MoO_6 loaded with different weight contents of Pt show an additional diffraction peak located at 39.75° of the (111) crystal plane of face center cubic (FCC) Pt structure with space group of Fm-3m (JCPDS No. 04-0802 [52]). Thus, the FCC Pt nanoparticles successfully coexisted with the orthorhombic Bi_2MoO_6 structure by a microwave-assisted deposition method. There was no detection of an impurity phase on the XRD pattern of the Bi_2MoO_6 sample, excluding the heterostructure Pt/Bi_2MoO_6 nanocomposites. The XRD patterns of as-prepared samples have a very high crystalline degree. Upon using the Scherrer equation, the crystallite size of Pt on heterostructure 10% Pt/Bi_2MoO_6 nanocomposites was about 18 nm [4, 53–56].

The Bi–O, Mo–O, and Mo–O–Mo bridging vibration modes of Bi_2MoO_6 were detected by FTIR (Fig. 3a) [11, 18, 20, 57, 58]. The Bi_2MoO_6 sample without the loaded Pt shows the weak peak located at 445 cm^{-1} related to the Bi–O stretching of the BiO_6 octahedron [11, 18, 20, 57, 58]. The FTIR peaks located at 726, 797, and 843 cm^{-1} correspond to the Mo–O stretching vibration of the MoO_6 octahedron [11, 18, 20, 57, 58]. Moreover, the FTIR peak at 572 cm^{-1} corresponds to the out-of-plane bending vibration of MoO_6 [11, 18, 20, 57, 58]. When Pt was loaded on the surface of the Bi_2MoO_6 sample, the FTIR vibration modes were similar to those of the pure Bi_2MoO_6 sample. The FTIR vibration modes of 10% Pt/Bi_2MoO_6 nanocomposites were slightly shifted to 447, 577, 731, 797, and 844 cm^{-1} because of the strong interaction of Pt and Bi_2MoO_6 nanoparticles. Additionally, broad FTIR peaks at approximately

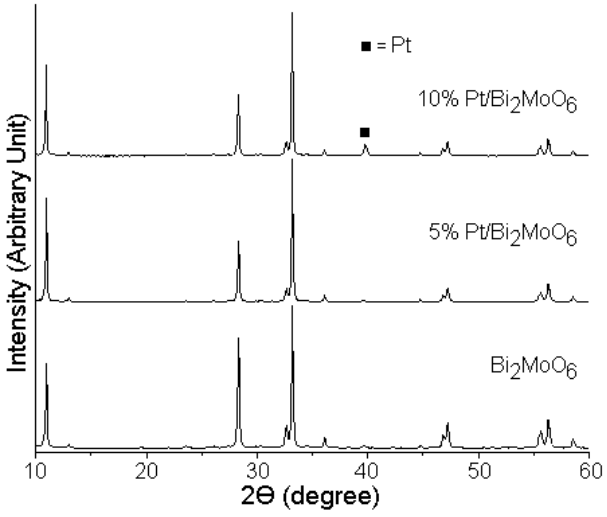

Figure 2. XRD patterns of Bi_2MoO_6 and heterostructure Pt/Bi_2MoO_6 samples.

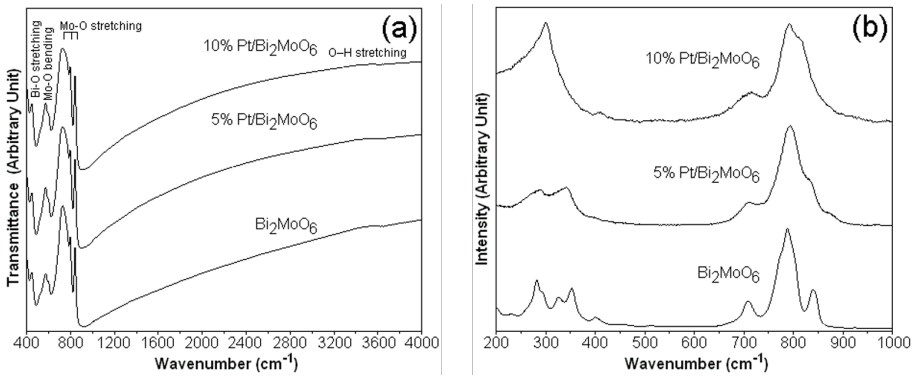

Figure 3. (a) FTIR and (b) Raman spectra of Bi_2MoO_6 and heterostructure Pt/Bi_2MoO_6 samples.

3200-3400 cm^{-1} were detected in all samples, which were ascribed to the O–H stretching vibration of adsorbed H_2O on the top surfaces [4, 5, 10, 11, 57, 58].

Fig. 3b shows the Raman spectra of as-prepared samples using Ar^+ as excitation wavelength at room temperature. The Raman spectrum of the pure Bi_2MoO_6 sample shows peaks at 282, 353, 709, 788, and 841 cm^{-1} . The weak Raman peaks at 282 and 353 cm^{-1} correspond to the symmetric stretching vibration of the Mo–O bond [1, 57–59]. Two Raman shoulders at 709 and 841 cm^{-1} correspond to the Mo–O stretching vibration of the MoO_6 octahedron [1, 9, 57–59]. The sharp Raman peak at 788 cm^{-1} was assigned to the symmetric Mo–O stretching vibration in the MoO_6 octahedron [1, 9, 57–59]. The Raman spectral intensity of 10% Pt/Bi_2MoO_6 nanocomposites was lower and wider than that of the pure Bi_2MoO_6 sample caused by the localized surface plasmon resonance (LSPR) of Pt nanoparticles and some defects of translational crystal symmetry of Pt/Bi_2MoO_6 nanocomposites [3, 60–62].

Fig. 4 shows SEM images of Bi_2MoO_6 without the loaded Pt and heterostructure 1%, 5%, and 10% Pt/Bi_2MoO_6 nanocomposites. The SEM image of the pure Bi_2MoO_6 sample was composed of a large number of nanoplates. The surface of Bi_2MoO6 nonaplates without the loaded Pt was smooth. The morphologies of the as-obtained heterostructure 1%, 5%, and 10 % Pt/Bi_2MoO_6 nanocomposites were similar to that of pure Bi_2MoO_6 samples. The uniform numerous Pt nanoparticles were loaded on the surface of Bi_2MoO_6 nanoplates. The metallic Pt nanoparticles played a role in improving the rate of photocatalytic reaction by charge carrier separation [9, 19, 28, 32, 32, 63, 64] . The loaded Pt nanoparticles on heterostructure 10% Pt/Bi_2MoO_6 nanocomposites were characterized by EDS as the result shown in Fig.S1. The nanocomposites were made up of Pt, Bi, Mo, and O, with a very good distribution of Pt on top of Bi_2MoO_6 nanoplates. The current result of heterostructure 10% Pt/Bi_2MoO_6 nanocomposites was in accordance with that of the above XRD analysis. The weight of Pt loaded on heterostructure 10% Pt/Bi_2MoO_6 nanocomposites was determined to be 8.32%. This result can lead to enhance the charge diffusion of Pt/Bi_2MoO_6 nanocomposites and the rate of photocatalytic reaction.

The morphology and structural characteristics of pure Bi_2MoO_6 sample and heterostructure 10% Pt/Bi_2MoO_6 nanocomposites were further examined by TEM. A typical TEM image of a pure Bi_2MoO_6 sample (Fig. 5a)

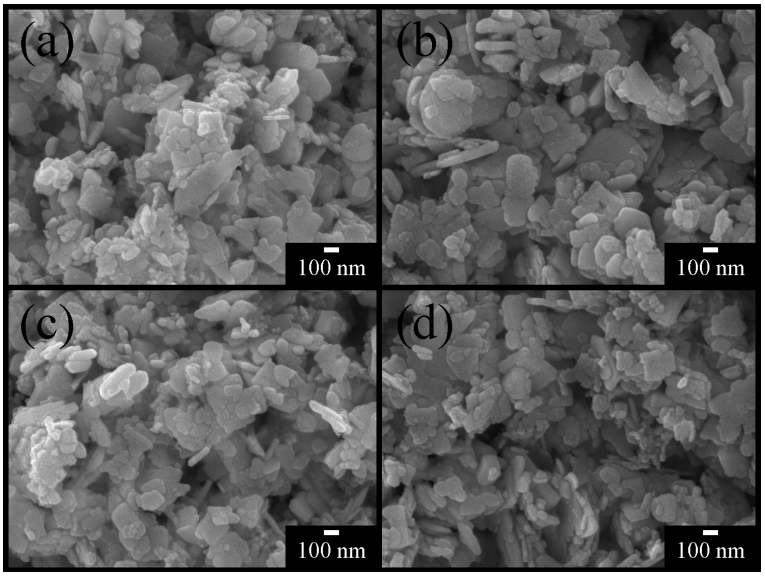

Figure 4. SEM images of (a) Bi_2MoO_6, (b) 1% Pt/Bi_2MoO_6, (c) 5% Pt/Bi_2MoO_6 and (d) 10% Pt/Bi_2MoO_6.

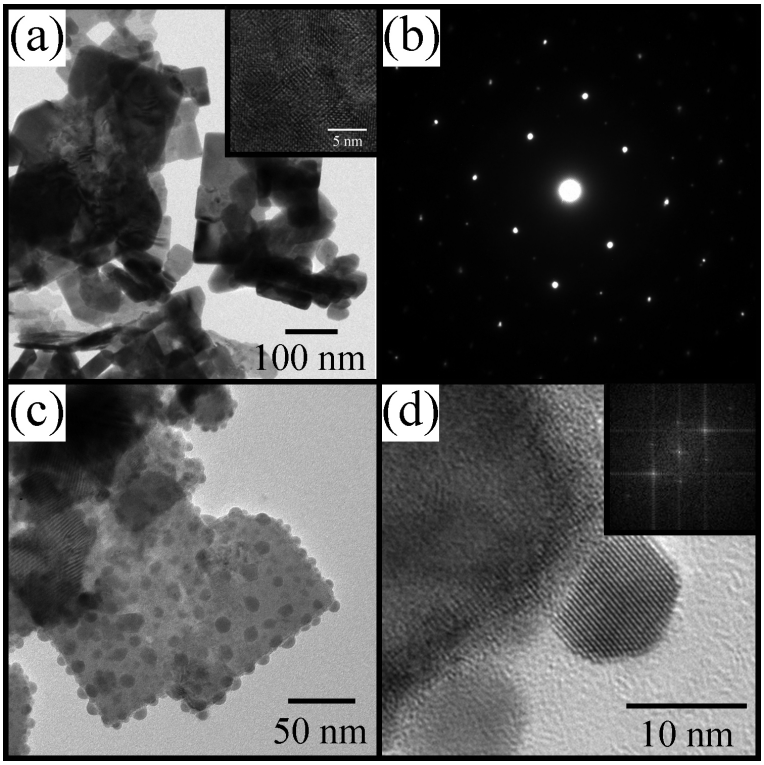

Figure 5. TEM and HRTEM images, SAED pattern and FFT pattern of (a, b) Bi_2MoO_6 and (c, d) heterostructure 10% Pt/Bi_2MoO_6 nanocomposites.

shows a number of nanoplates with a diameter of 100–200 nm. The high-resolution transmission electron microscopic (HRTEM) image of Bi_2MoO_6 nanoplates (inset of Fig. 5a) presents the spaces of (200) and (022) planes of orthorhombic Bi_2MoO_6 crystal. The selected area electron diffraction (SAED) pattern of a Bi_2MoO_6 nanoplate (Fig. 5b) shows the light spots of the electron diffraction pattern, which was indexed to the (060), (062), and (002) planes of orthorhombic Bi_2MoO_6 structure (JCPDS No. 21-0102 [52]). Fig. 5c shows the TEM image at high magnification of heterostructure 10% Pt/Bi_2MoO_6 nanocomposites. This image shows the full decoration of Pt spherical nanoparticles on top of Bi_2MoO_6 nanoplates. The Pt nanoparticles loaded on 1% Pt/Bi_2MoO_6 nanoparticles (Fig. S2) present the symmetric distribution of nanoparticles with a size of 3–11.4 nm. The average Pt nanoparticles of 10% Pt/Bi_2MoO_6 nanocomposites were 7.23 $\pm$1.28 nm. The high-resolution TEM (HRTEM) image of heterostructure 10% Pt/Bi_2MoO_6 nanocomposites (Fig. 5d) presents the heterojunction of Pt nanoparticles and Bi_2MoO_6 nanoplates with the lattice fringes of Pt nanoparticles and Bi_2MoO_6 nanoplates. This image shows the space of 0.227 nm of the (111) plane of FCC Pt (JCPDS No. 04-0802) [52] and those of 0.274 nm and 0.262 nm corresponding to the (200) and (022) planes of orthorhombic Bi_2MoO_6 nanoplates (JCPDS No. 21-0102 [52]), respectively. They certified that the Bi_2MoO_6 nanoplates were covered with Pt nanoparticles to form Pt/Bi_2MoO_6 heterojunctions, which played the role in promoting the effective separation of electrons and holes [6, 10, 12, 20, 29, 48, 49]. The Fast Fourier Transformation (FFT) of an individual Pt nanoparticle (inset of Fig. 5d) appears as a systematic diffraction pattern, which indicates the existence of a metallic Pt single crystal. The surface chemical state and interaction of Pt/Bi_2MoO_6 heterojunction were analyzed by XPS. The full-scale XPS spectra of Fig. 6a were composed of Bi, Mo, O, and C elements for Bi_2MoO_6 and Pt, Bi, Mo, O, and C elements for heterojunction 10% Pt/Bi_2MoO_6 nanocomposites. The carbon peak was caused by the contamination of the samples. Fig. 6b is the high-resolution XPS binding energies of Pt 4f core levels containing 10% Pt/Bi_2MoO_6. They were detected at 71.3 eV and 74.5 eV with the spin energy separation of 3.2 eV. The first corresponds with Pt $4f_{7/2}$, and the second corresponds with Pt $4f_{5/2}$ of metallic Pt^0 [63, 65, 66]. Thus, the Pt^{4+} ions were reduced to Pt^0 by microwaving with ethylene glycol as a reducing reagent. Moreover, the lower peaks for the binding energies of Pt 4f core levels at 72.5 eV (Pt $4f_{7/2}$) and 75.5 eV (Pt $4f_{5/2}$) with the spin energy separation of 3.0eV of Pt^{2+}. Thus, some Pt^0 is contained in the nanocomposites [63, 65, 66]. The high-resolution binding energy peaks of Bi 4f located at 159.45 eV and 164.76 eV for Bi_2MoO_6 and 159.52 eV and 164.83 eV for 10% Pt/Bi_2MoO_6 (Fig. 6c) correspond to Bi $4f_{7/2}$ and Bi $4f_{5/2}$ core levels, respectively. Thus, Bi species containing in Bi_2MoO_6 and heterojunction Pt/Bi_2MoO_6 nanocomposites exist in the form of Bi^{3+} [9–11, 18–20, 29, 32, 33, 57, 58]. Fig. 6d shows the high-resolution binding energies of Mo 3d core levels at 235.87eV of Bi_2MoO_6 and 235.92eV of 10% Pt/Bi_2MoO_6 for Mo $3d^{3/2}$ and 232.74eV of Bi_2MoO_6 and 232.76 eV of 10% Pt/Bi_2MoO_6 for Mo $3d^{5/2}$, indicating the existence of Mo^{6+} oxidation state inside the samples [9–11, 18–20, 29, 32, 33, 58, 59]. Fig. 6e shows the

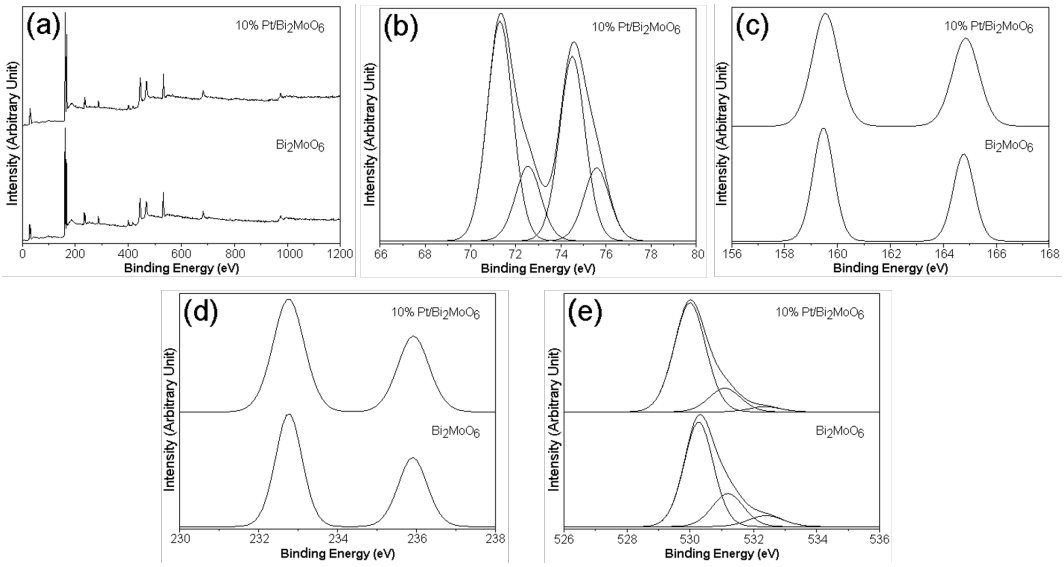

Figure 6. XPS spectra of (a) full survey scan, (b) Pt 4f, (c) Bi 4f, (d) Mo 3d, (e) O 1s of as-prepared Bi_2MoO_6 and heterostructure 10% Pt/Bi_2MoO_6 samples.

asymmetric high-resolution binding energy of the O 1s peak, which can be divided into three symmetric binding energy peaks of Bi_2MoO_6 and 10% Pt/Bi_2MoO_6 samples. They were attributed to the presence of $[Bi_2O_2]^{2+}$ (530.26 eV for Bi_2MoO_6 and 529.96 eV for 10% Pt/Bi_2MoO_6), adsorbed OH(531.17eV for Bi_2MoO_6 and 531.06 eV for 10% Pt/Bi_2MoO_6) and adsorbed H_2O (532.37 eV for Bi_2MoO_6 and 532.33 eV for 10% Pt/Bi_2MoO_6) [9, 11, 18–20, 29, 32, 33, 57, 58].

The optical properties of Bi_2MoO_6 without the loaded Pt and heterostructure Pt/Bi_2MoO_6 nanocomposites were studied by DRS over the 200–800 nm wavelength as the results shown in Fig. 7. Pure Bi_2MoO_6 nanoplates show the excellent UV-visible absorption which is attributed to the band gap transition of Mo 4d orbital and Bi 6p orbital as conduction band and O 2p orbital as valence band of Bi_2MoO_6.

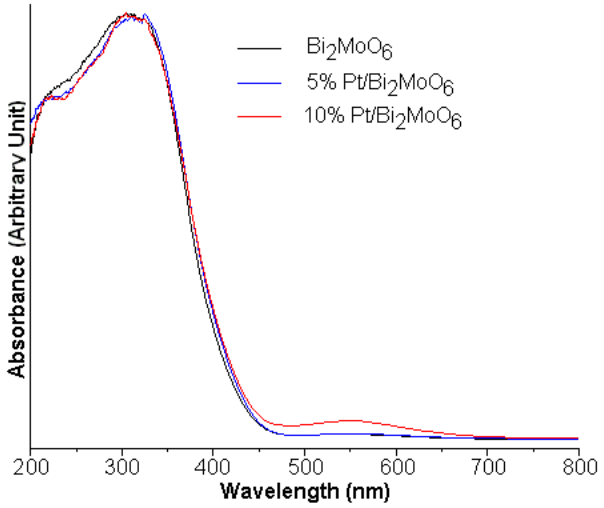

Figure 7. DRS spectra of as-prepared Bi_2MoO_6 sample, 5% Pt/Bi_2MoO_6 nanocomposites and 10% Pt/Bi_2MoO_6 nanocomposites.

The absorption edge of pure Bi_2MoO_6 nanoplates was detected at 441 nm. Thus, the pure Bi_2MoO_6 nanoplates played a role in harvesting the visible light catalytic activity [1, 9, 11, 17, 18, 29, 32, 33]. The heterostructure Pt/Bi_2MoO_6 nanocomposites have visible light absorption higher than pure Bi_2MoO_6 nanoplates. The visible light absorption of heterostructure 5% and 10% Pt/Bi_2MoO_6 nanocomposites was shifted towards the higher absorption edges of 445 nm and 447 nm, respectively. The loaded Pt nanoparticles played the role of improving visible light harvesting and enhancing the visible-light-driven photocatalytic reaction [9, 28, 29, 32, 33, 36]. They should be noted that heterostructure 10% Pt/Bi_2MoO_6 nanocomposites have additional broad absorption peak at 480-660 nm due to the surface plasmon resonance (SPR) absorption of the loaded Pt nanoparticles. Thus, the formation of heterojunction can greatly enhance visible-light absorption [9, 28, 29, 32, 33, 36, 63]. The band gap energy (E_g) of Bi_2MoO_6 without the loaded Pt and heterostructure Pt/Bi_2MoO_6 nanocomposites was calculated using $E_g = 1240/\lambda$. The obtained E_g values were 2.81, 2.78, and 2.77 eV for 0%, 5%, and 10% Pt/Bi_2MoO_6 nanocomposites, respectively [11, 29, 67, 68]. The band gap energy of heterostructure Pt/Bi_2MoO_6 nanocomposites was narrower than the band gap energy of Bi_2MoO_6 without the loaded Pt. The loaded Pt nanoparticles on Bi_2MoO_6 nanoplates can play the role in increasing the visible absorption range and enhancing the photocatalytic performance of Bi_2MoO_6 [9, 28, 29, 32, 33, 36]. The conduction band E_{CB} and valence band E_{VB} energies of as-prepared Bi_2MoO_6 nanoplates were calculated by the following Eqs. 2 and 3

$$E_{VB} = X - E_e + 0.5E_g \quad (2)$$

$$E_{CB} = E_{VB} - E_g \quad (3)$$

where X (5.55 eV for Bi_2MoO_6) is the Mulliken electronegativity theory, E_e is the energy of free electron on the hydrogen scale (4.50 eV), and E_g is the energy band gap [69–

72]. The calculated E_{VB} and E_{CB} of as-prepared Bi_2MoO_6 nanoplates were 2.45 eV and –0.36 eV, respectively.

Fig. 8 shows the nitrogen adsorption-desorption isotherms of Bi_2MoO_6 and 10% Pt/Bi_2MoO_6 nanocomposites. According to IUPAC classification, these adsorption-desorption isotherms correspond to the IV type with H3 type hysteresis loop of mesoporous material with aggregates of plate-like particles scattered in all directions giving rise to pores [12, 73–76]. The specific surface areas of Bi_2MoO_6 and heterostructure 10% Pt/Bi_2MoO_6 nanocomposites calculated by the BET method were 5.35 and 5.89 m^2/g, respectively. It should be noted that the loaded Pt nanoparticles on top of Bi_2MoO_6 nanoplates played a role in raising the specific surface area for photocatalytic reaction resulting from the increase of roughness of Bi_2MoO_6 nanoplates according to the SEM and TEM analyses. Thus, the photodegradation efficiency of the nanocomposites was enhanced [10, 11, 17, 18, 20, 77].

3.2 Photocatalytic reaction of heterostructure Pt/Bi_2MoO_6 nanocomposites

Fig. 9 shows the temporal evolution spectra for the photodegradation of RhB solution over heterostructure 10% Pt/Bi_2MoO_6 nanocomposites under visible illumination. The intensity at the (λ_{max}=554 nm) of RhB degradation photocatalyzed by heterostructure 10% Pt/Bi_2MoO_6 nanocomposites was gradually decreased. The spectral peaks were hypsochromic shifted to 498 nm caused by the formation of a series of N deethylated intermediates in a stepwise manner to N, N, N'triethylated rhodamine(λ_{max}=539nm), N, N'diethylated rhodamine(λ_{max}=522nm), N-ethylated rhodamine (λ_{max}=510 nm) and rhodamine (λ_{max}=498 nm) [17, 19, 34, 57, 58, 78, 79]. The color of the RhB suspension was sequentially changed from pink to light green and to a colorless solution. The absorption of RhB photocatalyzed by heterostructure 10% Pt/Bi_2MoO_6 nanocomposites was turned into zero at the end of 150 min. In the end, RhB was degraded into small molecules. The degradation of RhB photocatalyzed by heterostructure 10% Pt/Bi_2MoO_6 nanocomposites under visible illumination at different time intervals was analyzed by MS as the results shown in Fig. 10. At 60 min irradiation time, the intensity of m/z at 443.23 of RhB was very little, comparing with that at 0 min. The RhB molecules were degraded and transformed into the N, N, N'triethylated rhodamine (m/z = 415.20), N, N'diethylated rhodamine (m/z = 387.17), N-ethylated rhodamine (m/z = 359.13) and rhodamine (m/z = 331.10), corresponding to N deethylated of the RhB xanthene ring [80–82]. At 120 min irradiation time interval, the conjugated xanthene became cleavage structure, and the benzene ring structure was open, including the existence of intermediates with low molecular weight aromatic, cyclic, and aliphatic organic

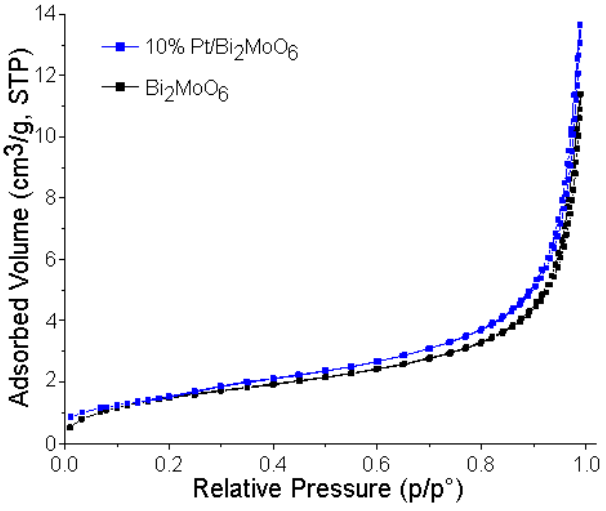

Figure 8. Nitrogen adsorption–desorption isotherm of $Bi_2MoO_6$and heterostructure 10% Pt/Bi_2MoO_6 samples.

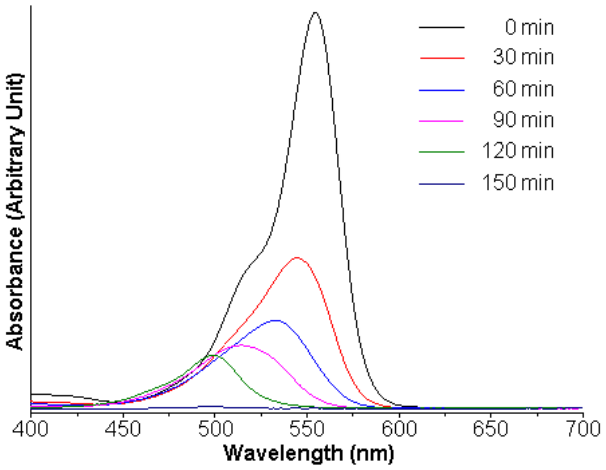

Figure 9. A temporal evolution of UV-visible spectra of RhB solutions photocatalyzed by10% Pt/Bi_2MoO_6 under visible light within 150 min.

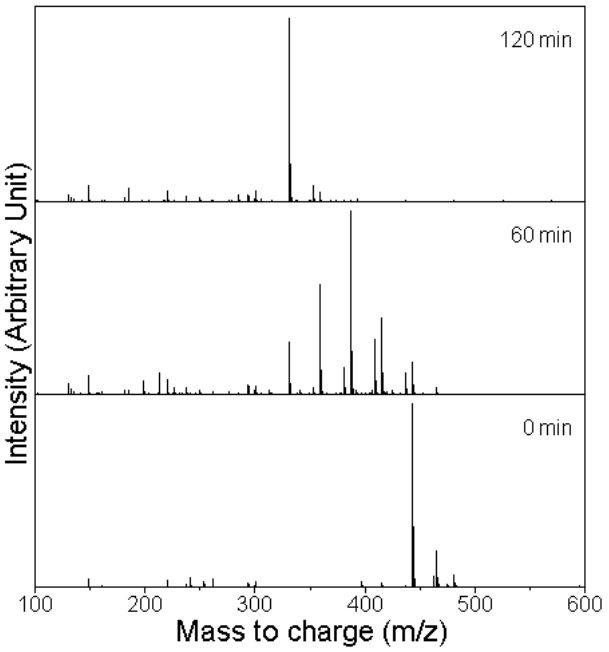

Figure 10. Mass spectra of RhB solutions photocatalyzed by 10% Pt/Bi_2MoO_6 under visible light within 0, 60 and 120 min.

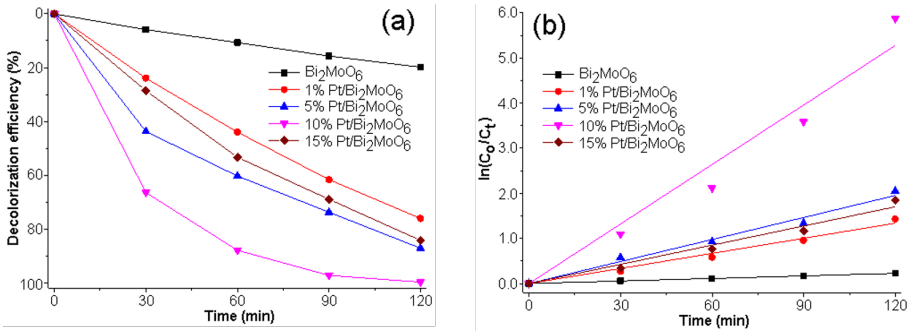

Figure 11. (a) Decolorization efficiencies and (b) pseudo-first-order plots for RhB degradation over heterostructure 0–15% Pt/Bi_2MoO_6 samples illuminated by visible light.

compounds such as benzoic acid, phthalic acid, bisphenol, 2−butoxyethanol and propane 1,2,3−triol [80–84].

According to the photodegradation efficiency shown in Fig. 11a, the photocatalytic efficiency for RhB degradation over Bi_2MoO_6 nanoplates was 19.86%. The photocatalytic efficiencies were increased to 76.09%, 87.15%, 99.76%, and 84.26% photocatalyzed by 1%, 5%, 10%, and 15% Pt/Bi_2MoO_6 nanocomposites, respectively. The photocatalytic efficiency of 10% Pt/Bi_2MoO_6 nanocomposites was the highest. The deposition of Pt nanoparticles has a significant influence on the photodegradation of RhB over Pt/Bi_2MoO_6 nanocomposites illuminated by visible radiation. The existence of Pt/Bi_2MoO_6 heterojunction played an important role in the separation and diffusion of charge carriers [76].

Thus, the heterostructure Pt/Bi_2MoO_6nanocomposites played a role in enhancing photocatalytic activity. The loaded Pt nanoparticles acted as electrical conductors for facilitating electron diffusion through the Schottky barrier between Pt nanoparticles and Bi_2MoO_6 nanoplates, including enhancing the separation of charge carriers [76]. The visible light absorption rate was increased by the SPR effect, and the photocatalytic reaction was increased [9, 19, 28, 32, 33, 63, 65, 66]. According to the previous reports [85–87], the efficiencies of oxide-semiconductor photocatalysts were greatly increased by the loaded rare metals due to the charge carrier separation by the Schottky barrier. Upon further increasing the loaded Pt nanoparticles to 15 wt%, the photocatalytic efficiency for RhB degradation was reduced to 84.26% because the Pt nanoparticles were agglomerated into Pt islands on the surface of Bi_2MoO_6 nanoplates as the result shown in Fig. S3. The photocatalytic efficiency of heterostructure 10% Pt/Bi_2MoO_6 nanocomposites is 5.02 times that of pure Bi_2MoO_6 nanoplates. The kinetic reaction over the Bi_2MoO_6 sample and Pt/Bi_2MoO_6 nanocomposites for RhB degradation under visible light can be calculated by the pseudo-first-order kinetic model below Eq. 4:

$$\ln(\frac{C_t}{C_0}) = -kt \quad (4)$$

where C_o and C_t are the contents of RhB at starting of the test and at time t, and k is the apparent reaction rate constant [2, 4, 11, 19, 24, 34, 58, 88, 89]. Fig. 11b shows the pseudo-first-order kinetic model for the degradation of RhB photocatalyzed by Bi_2MoO_6 nanoplates loaded with different weight contents of Pt nanoparticles illuminated by visible light. The photocatalytic reaction of all photocatalysts corresponds with the pseudo-first-order reaction kinetics with the correlation coefficient (R^2)0.95 [2, 4, 11, 19, 24, 34, 58]. Based on the pseudo-first-order kinetic model, the reaction rate constants for RhB degradation were 1.66×10^{-3}, 0.0112, 0.0161, 0.0437 and 0.0142 min^{-1} for 0%, 1%, 5%, 10% and 15% Pt/Bi_2MoO_6 nanocomposites, respectively. The reaction rate constant for RhB degradation was increased with an increase in the weight content of the loaded Pt to the highest of 10% and decreased with a further increase in the weight content of Pt of 15%. Clearly, the weight content of Pt is the key influence on the photodegradation of RhB under visible light. The reaction rate constant of the 10% Pt/Bi_2MoO_6 nanocomposites was about 26.33 times that of the pure Bi_2MoO_6 nanoplates. In summary, 10 wt%Pt loaded on Bi_2MoO_6 nanoplates is the best content for RhB degradation under visible light. The photocatalytic efficiency is higher than that of the previous reports (Table 1) [9, 11, 18–20, 29, 32–34, 57, 66]. Thus, Pt nanoparticles are the best candidate used to improve photocatalytic reactions. A scavenging experiment was processed to determine active species used to degrade RhB molecules. In this research, isopropyl alcohol (IPA), benzoquinone (BQ), and triethanolamine (TEOA) were added to the RhB solutions in order to trap hydroxyl radical (OH), superoxide radical (O_2^-) and hole (h^+), respectively [4, 10, 24, 29, 57, 58, 90, 91]. Fig. 12

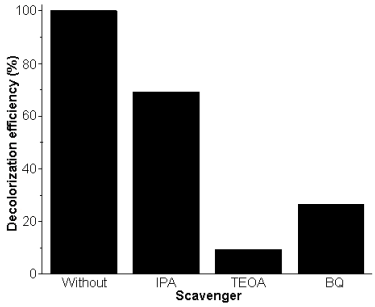

Figure 12. Photodegradation of RhB solutions with and without different scavengers over heterostructure 10% Pt/Bi_2MoO_6 nanocomposites illuminated by visible light.

Table 1. Photodegradation efficiencies of the present and other works in degrading toxic organic compounds.

Samples	Toxic organic Compounds	Degradation Efficiencies	References
Ag/Bi_2MoO_6	4-Nitrophenol (4-NP)	75% within 180 min	[9]
$UiO\text{-}66(Zr)/Bi_2MoO_6$	RhB	90% within 120 min	[11]
$g\text{-}C_3N_4/Bi_2MoO_6$	RhB	75% within 120 min	[18]
$5\%\ Pd/Bi_2MoO_6$	RhB	97.76% within 120 min	[19]
$3.5\%\ BN/Bi_2MoO_6$	Iohexol	90% within 150 min	[20]
$3\%\ Ag/Bi_2MoO_6$	RhB	74% within 120 min	[29]
$4\%\ Au/Bi_2MoO_6$	Phenol	73% within 3 h	[32]
$Au/Bi_2MoO_6@TiO_2$	Methylene blue (MB)	68% within 120 min	[33]
$10\%\ Ag/Bi_2MoO_6$	RhB	97.64% within 210 min	[34]
3% Au-doped Bi_2MoO_6	RhB	94.23% within 240 min	[57]
$Pt@CN/20\%\ Bi_2MoO_6$	MB	100% within 2 h	[66]
$10\%\ Pt/Bi_2MoO_6$	RhB	99.76% within 120 min	This work

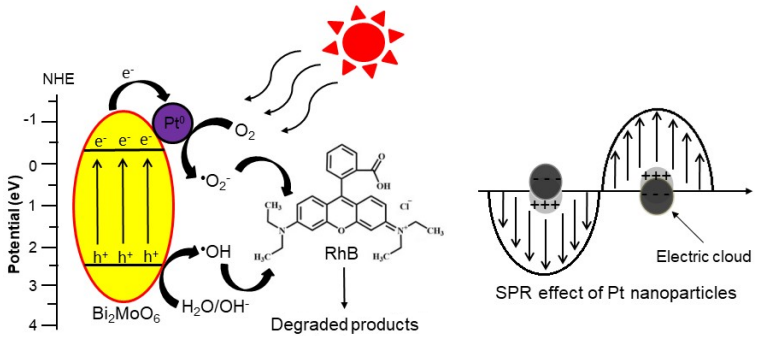

Figure 13. Photocatalytic mechanism of Pt/Bi_2MoO_6 for RhB degradation under visible light irradiation.

shows the photodegradation of RhB solutions with and without IPA, BQ, and TEOA photocatalyzed by heterojunctions of 10% Pt/Bi_2MoO_6 nanocomposites induced by visible light. The degradation efficiencies were significantly dropped to 9.35% and 26.38% for the addition of TEOA and BQ, respectively. The degradation efficiency was slightly dropped to 68.95% for the addition of IPA. These results reveal that h^+ and O_2^- were the main active species for the photodegradation of RhB molecules photocatalyzed by 10% Pt/Bi_2MoO_6 nanocomposites illuminated by visible radiation [24, 29, 57, 58, 73, 92]. Fig. 13 shows the photocatalytic mechanism of Pt/Bi_2MoO_6 for the degradation of RhB under visible light irradiation. The photo-excited electrons and photo-induced holes were in CB and VB of Bi_2MoO_6 under visible light irradiation [9, 19, 28, 32, 33, 63, 65, 66]. Hole (h^+) combined with H_2O/OH^- to form hydroxyl radical (OH). The loaded Pt nanoparticles acted as an electrical conductor. The separation of the electrons and holes was enhanced, the electric cloud was created, visible-light absorption was improved by the SPR effect, and the photocatalytic reaction was enhanced [9, 19, 28, 33, 63, 65, 66]. In the end, h+ and O_2^- radicals played the role in degrading and transforming RhB molecules into the degraded products [9, 19, 28, 32, 33, 63, 65, 66].

To evaluate the stability and reusability of 10% Pt/Bi_2MoO_6 nanocomposites, five-cycle degradation of RhB over 10% Pt/Bi_2MoO_6 nanocomposites induced by visible light was investigated as the results shown in Fig. 14. At the end of each photocatalytic reaction, 10% Pt/Bi_2MoO_6 nanocomposites were collected by centrifugation, washed and dried for the next photocatalytic reaction. At the end of the 5th cycle, the reused 10% Pt/Bi_2MoO_6 nanocomposites have

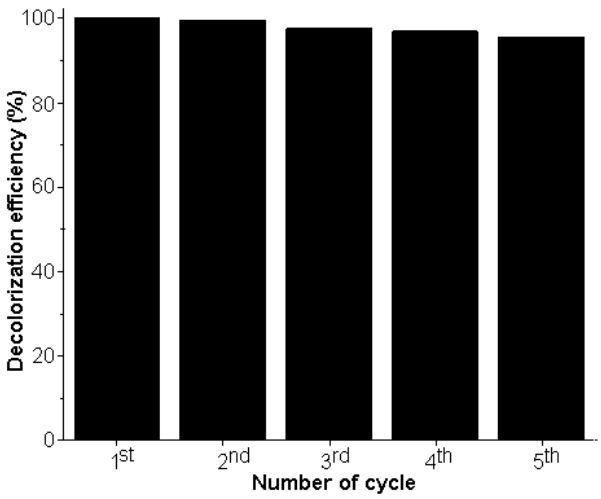

Figure 14. Photodegradation of RhB solutions photocatalyzed by reused 10% Pt/Bi_2MoO_6 nanocomposites within five cycles.

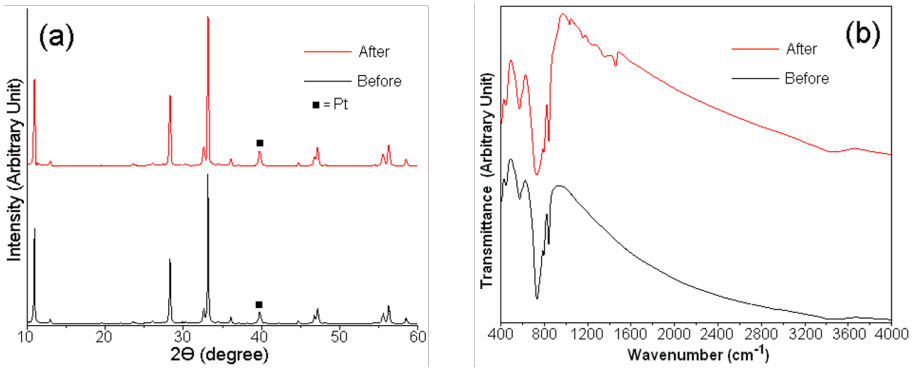

Figure 15. Comparison (a) XRD patterns and (b) FTIR spectra of 10% Pt/Bi_2MoO_6 at the beginning of the photocatalytic test and at the end of the 5^{th} cycle.

a high photocatalytic activity of 95.21%, which is slightly reduced with respect to the photocatalytic activity of the 1st cycle. Fig. 15 shows XRD and FTIR spectra of reused 10% Pt/Bi_2MoO_6 before a photocatalytic test and at the end of the 5th photocatalytic cycle. The XRD pattern of reused 10% Pt/Bi_2MoO_6 still corresponds with orthorhombic Bi_2MoO_6 structure (JCPDS No. 21-0102 [52]) as the main phase and FCC Pt structure (JCPDS No. 04-0802 [52]) as the minor phase. Thus, the phase and structure of Pt/Bi_2MoO_6 were highly stable. Nevertheless, the FTIR spectrum of reused 10% Pt/Bi_2MoO_6 shows a new FTIR peak around 1000-1400 cm^{-1} assigned to the vibration of RhB. It indicates that RhB was adsorbed on the surface of 10% Pt/Bi_2MoO_6 nanocomposites [93, 94]. Thus, the 10% Pt/Bi_2MoO_6 nanocomposites are very excellent photocatalytic material for the practical application.

4. Conclusions

Heterostructure Pt/Bi_2MoO_6 nanocomposites containing different contents of Pt nanoparticles were successfully synthesized by an effective microwave-assisted deposition method. The heterostructure Pt/Bi_2MoO_6 nanocomposites were composed of spherical metallic Pt nanoparticles loaded on the surface of Bi_2MoO_6 nanoplates. The heterostructure 10% Pt/Bi_2MoO_6 nanocomposites played a role in the best photocatalytic degradation of RhB under visible illumination due to the formation of the Schottky barrier of Pt nanoparticles and Bi_2MoO_6 nanoplates. These nanoparticles were excellently stable and reusable for wastewater treatment.

Acknowledgement
This research was supported by the National Science, Research and Innovation Fund (NSRF), Thailand, and Prince of Songkla University (grant no. SCI6701032S).

Authors Contributions
S. Pinchujit: Data curation, Formal analysis. A. Phuruangrat: Conceptualization, Methodology, Investigation, Data curation, Formal analysis, Supervision, Writing – review and editing. S. Wannapop: Formal analysis. T. Thongtem: Conceptualization, Formal analysis, Writing – review and editing. S. Thongtem: Conceptualization, Formal analysis, Writing – review and editing.

Availability of Data and Materials
Data is available on request from the corresponding author, upon reasonable request.

Conflict of Interests
The authors declare that they have no known competing financial interests or personal relationships that could have appeared to influence the work reported in this paper.

References

[1] Q. Zhao, M. Long, H. Li, L. Wang, X. Bai, Y. Zhang, and D. Li. *Cryst. Res. Technol.*, **56**(2021):2000219. DOI: https://doi.org/10.1002/crat.202000219.

[2] J. P. Shubha, N. V. Sushma, S. F. Adil, M. Khan, M. E. Assal, M. R. Hatshan, and B. Shaik. *J. King Saud Univ. Sci.*, **34**(2022):101738. DOI: https://doi.org/10.1016/j.jksus.2021.101738.

[3] M. Faisal, M.and Alsaiari, Md. A. Rashed, and F. A. Harraz. *J. Mater. Res. Technol*, **14**(2021):954–967. DOI: https://doi.org/10.1016/j.jmrt.2021.06.093.

[4] M. Yilmaz, N. Mengelizadeh, M. K. Saloot, S. Shahbaksh, and D. Balarak. *Mater. Sci. Semicond. Process.*, **144**(2022):106593. DOI: https://doi.org/10.1016/j.mssp.2022.106593.

[5] S. Zarezadeh, A. Habibi-Yangjeh, M. Mousavi, and S. Ghosh. *Mater. Sci. Semicond. Process*, **119**(2020):105229. DOI: https://doi.org/10.1016/j.mssp.2020.105229.

[6] L. Liang, L. Cheng, Y. Zhang, Q. Wang, Q. Wu, Y. Xue, and X. Meng. *RSC Adv.*, **10**(2020):28509. DOI: https://doi.org/10.1039/D0RA03125A.

[7] W. Lu, Q.and Gao, J. Du, L. Zhou, and Y. Lian. *J. Agric. Food Chem.*, **60**(2012):4773–4778. DOI: https://doi.org/10.1021/jf300067z.

[8] P. Zhou, Z. Dai, T. Lu, X. Ru, M. A. Ofori, W. Yang, J. Hou, and H. Jin. *Catalysts*, **12**(2022):669, . DOI: https://doi.org/10.3390/catal12060669.

[9] H. Shen, W. Xue, F. Fu, J. Sun, Y. Zhen, D. Wang, B. Shao, and J. Tang. *Chem. Eur. J.*, **24**(2018):18463–18478. DOI: https://doi.org/10.1002/chem.201804267.

[10] V. Shanmugam, A. L. Muppudathi, S. Jayavel, and K. S. Jeyaperumal. *Arabian J. Chem.*, **13**(2020):2439–2455. DOI: https://doi.org/10.1016/j.arabjc.2018.05.009.

[11] J. Ding, Z. Yang, C. He, X. Tong, Y. Li, X. Niu, and H. Zhang. *J. Colloid Interf. Sci.*, **497**(2017):126–133. DOI: https://doi.org/10.1016/j.jcis.2017.02.060.

[12] J. Zhang, Z. Chen, R. Guo, D. Shan, Y. Zhao, X. Linghu, Y. Shu, and B. Wang. *Arabian J. Chem.*, **15**(2022):103659. DOI: https://doi.org/10.1016/j.arabjc.2021.103659.

[13] P. Dhull, A. Sudhaik, V. Sharma, P. Raizada, V. Hasija, N. Gupta, T. Ahamad, V. H. Nguyen, A. Kim, M. Shokouhimehr, S. Y. Kim, Q. V. Le, and P. Singh. *Mol. Catal.*, **539**(2023):113013. DOI: https://doi.org/10.1016/j.mcat.2023.113013.

[14] A. A. P. Khan, P. Singh, P. Raizada, A. Khan, A. M. Asiri, and M. M. Alotaibi. *Chemosphere*, **316**(2023):137839. DOI: https://doi.org/10.1016/j.chemosphere.2023.137839.

[15] A. Kumar, P. Singh, V. H. Nguyen, Q. V. Le, T. Ahamad, S. Thakur, L. H. Nguyen, and P. Raizada. *Chem. Eng. J.*, **474**(2023):145720. DOI: https://doi.org/10.1016/j.cej.2023.145720.

[16] M. Rezaei and A. Nezamzadeh-Ejhieha. *Inter. J. Hydrog. Energ.*, **45**(2020):24749–24764. DOI: https://doi.org/10.1016/j.ijhydene.2020.06.258.

[17] M. Xu and W. D. Zhang. *Eur. J. Inorg. Chem.*, **2016**(2016):826–831. DOI: https://doi.org/10.1002/ejic.201501260.

[18] K. Xia, H. Chen, M. Mao, Z. Chen, F. Xu, J. Yi, Y. Yu, X. She, H. Xu, and H. Li. *Phys. Status Solidi A*, **215**(2018):1800520. DOI: https://doi.org/10.1002/pssa.201800520.

[19] A. Phuruangrat, T. Klangnoi, P. Patiphatpanya, P. Dumrongrojthanath, and S. Thongtem. *T. Thongtem, Optik*, **212**(2020):164674, . DOI: https://doi.org/10.1016/j.ijleo.2020.164674.

[20] H. He, W. Wang, C. Xu, S. Yang, C. Sun, X. Wang, Y. Yao, N. Mi, W. Xiang, S. Li, and G. Liu. *Sci. Total Environ.*, **730**(2020):139100. DOI: https://doi.org/10.1016/j.scitotenv.2020.139100.

[21] Y. Shi, S. Feng, and C. Cao. *Mater. Lett.*, **44**(2000): 215–218. DOI: https://doi.org/10.1016/S0167-577X(00)00030-6.

[22] C. Kongmark, R. Coulter, S. Cristol, A. Rubbens, C. Pirovano, A. Lofberg, G. Sankar, W. Beek, E. Bordes-Richard, and R. N. Vannier. *Cryst. Growth Des.*, **12**(2012):5994–6003. DOI: https://doi.org/10.1021/cg301070e.

[23] A. T. Adeleye, K. I. John, P. G. Adeleye, A. A. Akande, and O. O. Banjoko. *J. Mater. Sci.*, **56**(2021): 183291–18416. DOI: https://doi.org/10.1007/s10853-021-06473-1.

[24] J. Xue, C. Huang, Y. Zong, J. Gu, M. Wang, and S. Ma. *Appl. Organometal. Chem.*, **33**(2019):e5187. DOI: https://doi.org/10.1002/aoc.5187.

[25] M. Rezaei, A. Nezamzadeh-Ejhieh, and A. R. Massah. *Energ. Fuel.*, **38**(2024):7637–7664, . DOI: https://doi.org/10.1021/acs.energyfuels.4c00325.

[26] M. Rezaei, A. Nezamzadeh-Ejhieh, and A. R. Massah. *ACS Omega*, **9**(2024):6093–6127, . DOI: https://doi.org/10.1021/acsomega.3c07560.

[27] Z. Sun, X. Yang, X. Yu, L. F. Xia, Y. Peng, Z. Li, Y. Zhang, J. Cheng, K. Zhang, and J. Yu. *Appl. Catal. B*, **285**(2021):119790. DOI: https://doi.org/10.1016/j.apcatb.2020.119790.

[28] Y. Ma, Y. Jia, Y. Lin, and W. Shia. *Dalton Trans.*, **48**(2019):12009–12012, . DOI: https://doi.org/10.1039/C9DT02028D.

[29] Z. X. Dai, L. Y. Zhang, C. L. Ruan, Z. Q. Yun, and G. H. Zheng. *Dig. J. Nanomater. Bios.*, **17**(2022):179–191, . DOI: https://doi.org/10.15251/DJNB.2022.171.179.

[30] Y. Wu, M. Song, Z. Chai, and X. Wang. *Inorg. Chem.*, **58**(2019):7374–7384. DOI: https://doi.org/10.1021/acs.inorgchem.9b00524.

[31] G. Ren, S. Liu, Z. Li, H. Bai, X. Hu, and X. Meng. *Sol. RRL*, **6**(2022):2200154. DOI: https://doi.org/10.1002/solr.202200154.

[32] L. Guo, Q. Zhao, H. Shen, X. Han, K. Zhang, D. Wang, F. Fu, and B. Xu. *Catal. Sci. Technol.*, **9**(2019):3193–3202. DOI: https://doi.org/10.1039/C9CY00579J.

[33] J. Cai, J. Huang, and Y. Lai. *J. Mater. Chem. A*, **5**(2017):16412–16421. DOI: https://doi.org/10.1039/C7TA02077E.

[34] P. Suebsom, A. Phuruangrat, S. Suwanboon, S. Thongtem, and T. Thongtem. *Inorg. Chem. Commun.*, **119**(2020):108120. DOI: https://doi.org/10.1016/j.inoche.2020.108120.

[35] N. Mehrabanpour, A. Nezamzadeh-Ejhieh, S. Ghattavi, and A. Ershadi. *Appl. Surf. Sci.*, **614**(2023):156252. DOI: https://doi.org/10.1016/j.apsusc.2022.156252.

[36] X. Yang, Y. Wang, X. Xu, Y. Qu, X. Ding, and H. Chen. *Chinese J. Catal.*, **38**(2017):260–269. DOI: https://doi.org/10.1016/S1872-2067(16)62553-6.

[37] S. Dong, J. Wu, L. Huang, and H. E. Wang. *Crystals*, **12**(2022):778. DOI: https://doi.org/10.3390/cryst12060778.

[38] J. J. Zou, C. J. Liu, K. L. Yu, D. G. Cheng, Y. P. Zhang, F. He, H. Y. Du, and L. Cui. *Chem. Phys. Lett.*, **400**(2004):520–523. DOI: https://doi.org/10.1016/j.cplett.2004.11.003.

[39] J. Li, Y. Yan, G. Sun, J. Yang, Z. Wang, and X. Yan. *Quim. Nova.*, **44**(2021):295–300, . DOI: https://doi.org/10.21577/0100-4042.20170685.

[40] H. Liu, H. Liu, J. Yang, H. Zhai, X. Liu, and H. Jia. *Cera. Inter.*, **45**(2019):20133–20140, . DOI: https://doi.org/10.1016/j.ceramint.2019.06.279.

[41] M. H. Wang, H. L. Cai, Z. L. Guo, Q. A. Qiao, S. H. Ren, D. D. Zhu, and Z. X. Xue. *Micro Nano Lett.*, **14**(2019):656–660, . DOI: https://doi.org/10.1049/mnl.2018.5308.

[42] A. Phuruangrat, T. Thongtem, and S. Thongtem. *Inorg. Nano-Met. Chem.*, **51**(2021):1813–1821, . DOI: https://doi.org/10.1080/24701556.2020.1855198.

[43] S. W. Chook, C. H. Chia, S. Zakaria, M. K. Ayob, K. L. Chee, N. M. Huang, H. M. Neoh, H. N. Lim, R. Jamal, and R. M. F. R. A. Rahman. *Nanoscale Res. Lett.*, **7**(2012):541. DOI: https://doi.org/10.1186/1556-276X-7-541.

[44] J. D. Xie, S. Gu, and H. Zhang. *Sensors*, **17**(2017): 2163, . DOI: https://doi.org/10.3390/s17102163.

[45] O. Koikolainen, L. Sondermann, S. Roitsch, I. Simon, D. Dietrich, V. Gvilava, J. Barthel, J. Thomas, C. Janiak, and I. Boldog. *J. Mater. Chem. A*, **10**(2022):11955–11970. DOI: https://doi.org/10.1039/D2TA00883A.

[46] M. Marcinek, X. Song, and R. Kostecki. *Electrochem. Commun.*, **9**(2007):1739–1743. DOI: https://doi.org/10.1016/j.elecom.2007.03.030.

[47] E. H. Jo, H. Chang, S. K. Kim, J. H. Choi, S. R. Park, C. M. Lee, and H. D. Jang. *Sci. Rep.*, **6**(2016):33236. DOI: https://doi.org/10.1038/srep33236.

[48] I. Durasovic, G. Stefanic, G. Drazic, R. Peter, Z. Klencsar, M. Marcius, T. Jurkin, S. Ivanda, M. an Stichleutner, and M. Gotic. *Nanomaterials*, **13**(2023):2418. DOI: https://doi.org/10.3390/nano13172481.

[49] C. T. Hsieh, W. Y. Chen, I. Chen, and A. K. Roy. *J. Power Sources*, **199**(2012):94–102. DOI: https://doi.org/10.1016/j.jpowsour.2011.10.055.

[50] E. Gabano and M. Ravera. Microwave-assisted synthesis: Can transition metal complexes take advantage of this "green" method? *Molecules*, **27**(2022):4249. DOI: https://doi.org/10.3390/molecules27134249.

[51] Y. J. Zhu and F. Chen. *Chem. Rev.*, **114**(2014):6462–6555. DOI: https://doi.org/10.1021/cr400366s.

[52] Powder Diffract. *File, JCPDS-ICDD,*, **12**(2001) (Campus Blvd., Newtown Square, PA , U.S.A.):19073–3273.

[53] A. B. Shishmakov, Yu. V. Mikushina, O. V. Koryakova, and L. A. Petrov. *Russ. J. Inorg. Chem.*, **64**(2019):864–869. DOI: https://doi.org/10.1134/S0036023619070155.

[54] A. Haghighatzadeh, M. Hosseini, S. Haghighi, and M. A. Dil. *J. Aust. Ceram. Soc.*, **57**(2021):993–1002. DOI: https://doi.org/10.1007/s41779-021-00602-4.

[55] N. Deilami and A. Haghighatzadeh. *J. Aust. Ceram. Soc.*, **57**(2021):409–418. DOI: https://doi.org/10.1007/s41779-020-00553-2.

[56] H. Hassani, S. Ebrahim, and N. Feizi. *Russ. J. Inorg. Chem.*, **65**(2020):940–947. DOI: https://doi.org/10.1134/S0036023620060054.

[57] A. Phuruangrat, S. Buapoon, T. Bunluesak, P. Suebsom, S. Wannapop, T. Thongtem, and S. Thongtem. *J. Aust. Ceram. Soc.*, **58**(2022):999–1008, . DOI: https://doi.org/10.1007/s41779-022-00765-8.

[58] A. Phuruangrat, S. Buapoon, T. Bunluesak, P. Suebsom, S. Thongtem, and T. Thongtem. *J. Aust. Ceram. Soc.*, **58**(2022):71–82, . DOI: https://doi.org/10.1007/s41779-021-00665-3.

[59] H. H. Li, C. Y. Liu, K. W. Li, and H. Wang. *J. Mater. Sci.*, **43**(2008):7026–7034, . DOI: https://doi.org/10.1007/s10853-008-3034-y.

[60] A. L. Cook, C. P. Haycook, A. K. Locke, R. R. Mu, and T. D. Giorgio. *Nanoscale Adv.*, **3**(2021):407. DOI: https://doi.org/10.1039/D0NA00563K.

[61] J. Yin, Y. Zang, C. Yue, Z. Wu, S. Wu, J. Li, and Z. Wu. *J. Mater. Chem.*, **22**(2012):7902–7909. DOI: https://doi.org/10.1039/C2JM16003J.

[62] P. T. Thuy, V. C. Minh, V. Q. Mai, N. T. Tuan, P. V. Tuan, H. B. Cuong, and N. X. Sang. *J. Nanomater.*, **2021**(2021):3806691. DOI: https://doi.org/10.1155/2021/3806691.

[63] H. Zhu, Y. Ji, L. Chen, W. Bian, and J. Wang. *Catalysts*, **10**(2020):206. DOI: https://doi.org/10.3390/catal10020206.

[64] A. D. Mauro, M. Zimbone, M. Scuderi, G. Nicotra, M. E. Fragala, and G. Impellizzeri. *Nanoscale Res. Lett.*, **10**(2015):484. DOI: https://doi.org/10.1016/j.jcis.2022.08.048.

[65] S. M. Albukhari, A. A. Ismail, S. Z. Alsheheri, and M. H. H. Mahmoud. *Inter. J. Environ. Sci. Tech.*, **19**(2022):7067–7078. DOI: https://doi.org/10.1007/s13762-021-03825-x.

[66] Z. Jia, F. Lyu, L. C. Zhang, S. Zeng, S. X. Liang, Y. Y. Li, and J. Lu. *Sci. Rep.*, **9**(2019):7636. DOI: https://doi.org/10.1038/s41598-019-42973-6.

[67] B. Y. Wang, E. D. Li, Y. C. Zong, X. B. Wang, J. Yuan, and F. Q. Zhang. *J. Mater. Res.*, **37**(2022):1070–1082, . DOI: https://doi.org/10.1557/s43578-022-00513-5.

[68] M. Hosseini-Sarvari and A. M. Sarvestani. *Photochem. Photobio. Sci.*, **20**(2021):903–911. DOI: https://doi.org/10.1007/s43630-021-00068-0.

[69] H. Li, Q. Deng, J. Liu, W. Hou, N. Du, R. Zhang, and X. Tao. *Catal. Sci. Technol.*, **4**(2014):1028–1037, . DOI: https://doi.org/10.1039/C3CY00940H.

[70] S. Li, Y. Liu, Y. Long, L. Mo, H. Zhang, and J. Liu. *Catalysts*, **8**(2018):447, . DOI: https://doi.org/10.3390/catal8100477.

[71] Z. X. Dai, L. Y. Zhang, C. L. Ruan, Z. Q. Yun, and G. H. Zheng. *Dig. J. Nanomater. Bios.*, **17**(2022):179–191, . DOI: https://doi.org/10.15251/DJNB.2022.171.179.

[72] A. A. Nada, M. Nasr, R. Viter, P. Miele, S. Roualdes, and M. Bechelany. *J. Phys. Chem. C*, **121**(2017):24677–24669, . DOI: https://doi.org/10.1021/acs.jpcc.7b08567.

[73] X. Liu, W. Y. Huang, Q. Zhou, X. R. Chen, K. Yang, D. Li, and D. D. Dionysiou. *Rare Met.*, **40**(2021):1086–1098, . DOI: https://doi.org/10.1007/s12598-020-01574-3.

[74] Y. Gao, L. Li, W. Zu, Y. Sun, J. Guan, Y. Cao, H. Yu, and W. Zhang. *J. Inorg. Organomet. Polym. Mater.*, **32**(2022):1840–1852. DOI: https://doi.org/10.1007/s10904-022-02242-y.

[75] S. Ghattavi and A. Nezamzadeh-Ejhieh. *Compos. B*, **183**(2020):107712. DOI: https://doi.org/10.1016/j.compositesb.2019.107712.

[76] B. Liu, C. Bie, Y. Zhang, L. Wang, Y. Li, and J. Yu. *Langmuir*, **37**(2021):14114–14124, . DOI: https://doi.org/10.1021/acs.langmuir.1c02360.

[77] R. Wang, M. Shi, F. Xu, Y. Qiu, P. Zhang, K. Shen, Q. Zhao, J. Yu, and Y. Zhang. *Nat. Commun.*, **11**(2020):4465, . DOI: https://doi.org/10.1038/s41467-020-18267-1.

[78] A. Barras, S. Cordier, and R. Boukherroub. *Appl. Catal. B*, **123-124**(2012). DOI: https://doi.org/10.1016/j.apcatb.2012.04.006.

[79] M. Wang, Z. Qiao, M. Fang, Z. Huang, Y. Liu, X. Wu, C. Tang, H. Tang, and H. Zhu. *RSC Adv.*, **5**(2015):94887–94894, . DOI: https://doi.org/10.1039/C5RA19164E.

[80] Z. Wang, L. Xia, J. Chen, L. Ji, Y. Zhou, Y. Wang, L. Cai, J. Guo, and W. Song. *Catalysts*, **10**(2020):1130, . DOI: https://doi.org/10.3390/catal10101130.

[81] S. Rajalakshmi, S. Pitchaimuthu, N. Kannan, and P. Velusamy. *Appl. Water Sci.*, **7**(2017):115–127. DOI: https://doi.org/10.1007/s13201-014-0223-5.

[82] M. Zhou, X. Tian, H. Yu, Z. Wang, C. Ren, L. Zhou, Y. W. Lin, and L. Dou. *ACS Omega*, **6**(2021):26439–26453, . DOI: https://doi.org/10.1021/acsomega.1c03694.

[83] D. Ma, J. Tang, G. He, and S. Pan. *Materials*, **17**(2024), . DOI: https://doi.org/10.3390/ma17040957.

[84] R. Xie, K. Fang, Y. Liu, W. Chen, J. Fan, X. Wang, Y. Ren, and Y. Song. *J. Mater. Sci.*, **55**(2020):11919–11937, . DOI: https://doi.org/10.1007/s10853-020-04863-5.

[85] A. A. Nada, B. O. Orimolade, H. H. El-Maghrabi, B. A. Koiki, M. Rivallin, M. F. Bekheet, R. D. Viter, Damberga, G. Lesage, I. Iatsunskyi, E. Coy, M. Cretin, O. A. Arotiba, and M. Bechelany. *Appl. Mater. Today*, **24**(2021):101129, . DOI: https://doi.org/10.1016/j.apmt.2021.101129.

[86] H. R. Tantawy, A. A. Nada, A. Baraka, and M. A. Elsayed. *Appl. Surf. Sci. Adv.*, **3**(2021):100056. DOI: https://doi.org/10.1016/j.apsadv.2021.100056.

[87] M. Rehan, A. A. Nada, T. A. Khattab, N. A. M. Abdelwahed, and A. A. A. El-Kheir. *J. Mater. Res. Technol.*, **9**(2020):9380–9394. DOI: https://doi.org/10.1016/j.jmrt.2020.05.079.

[88] A. Yousefi and A. Nezamzadeh-Ejhieh. *Iran. J. Catal.*, **11**(2021):247–259.

[89] A. Nezamzadeh-Ejhieh and M. Karimi-Shamsabadi. *Chem. Eng. J.*, **228**(2013):631–641. DOI: https://doi.org/10.1016/j.cej.2013.05.035.

[90] Y. Ma, C. Lv, J. Hou, S. Yuan, Y. Wang, P. Xu, G. Gao, and J. Shi. *Nanomaterials*, **9**(2019):322, . DOI: https://doi.org/10.3390/nano9030322.

[91] B. Niu and Z. Xu. *Green Chem.*, **21**(2019):874–884. DOI: https://doi.org/10.1039/C8GC02263A.

[92] S. A. Mirsalari and A. Nezamzadeh-Ejhieha. *Sep. Purif. Technol.*, **250**(2020):117235. DOI: https://doi.org/10.1016/j.seppur.2020.117235.

[93] W. Kang, Y. Gao, X. Tang, C. Cao, L. Hu, and H. Yang. *J. Appl. Polym. Sci.*, **136**(2019):47468. DOI: https://doi.org/10.1002/app.47468.

[94] Z. Jiang, B. Dong, B. Chen, J. Wang, L. Xu, S. Zhang, and H. Song. *Small*, **9**(2013):604–612. DOI: https://doi.org/10.1002/smll.201201558.